Int J Adv Manuf Technol (2018) 94:463–474
DOI 10.1007/s00170-017-0736-9

ORIGINAL ARTICLE

Physically based modeling method for comprehensive thermally induced errors of CNC machining centers

Kuo Liu[1] · **Tiejun Li**[2] · **Yongqing Wang**[1] · **Mingjia Sun**[3] · **Yuliang Wu**[3] · **Tiejun Zhu**[3]

Received: 20 February 2017 / Accepted: 26 June 2017 / Published online: 12 August 2017

Abstract The advantages of PBM (physically based model) over DDM (data-driven model) were presented, and physically based modeling of comprehensive thermal errors of servo axis and spindle was proposed. Based on the theory of frictional heat, heat convection, and heat conduction, the model for thermal error of servo axis was established, and the screw temperature field at any time can be obtained to predict screw thermal error. The thermal bending deformations of spindles were analyzed for a C-type vertical machining center. The models for spindle radial thermal drift error under different deformations were established, and the criterion for determining the deformations was presented. Tests for identifying parameters of the suggested models were carried out on a TC500R vertical machining center. The compensation effects were verified using both experiment and machining. The results indicated that the suggested PBM results in high accuracy and strong robustness, even if the moving state of servo axis and the rotating speed of spindle randomly changed.

Keywords Vertical machining center · Physically based model · Comprehensive thermal error · Compensation

✉ Yongqing Wang
yongqing_wang1969@126.com

[1] Key Laboratory for Precision and Non-traditional Machining Technology of Ministry of Education, Dalian University of Technology, Dalian 116024, China

[2] College of Mechanical Engineering and Automation, Northeastern University, Shenyang 110819, China

[3] State Key Laboratory, Shenyang Machine Tool (Group) CO., LTD, Shenyang 110142, China

1 Introduction

The temperature rise of machine tools due to both inner and outer sources [1, 2] can cause changes of distance between the workpiece and the cutter, thus leading to machining errors [3]. The inner heat source includes motors, friction kinematic pairs, cutting heat, and coolant; the outer heat source includes environment, lightning, and human. Thermally induced errors account for about 40–70% of the total errors of a machine tool and seriously influence the machining accuracy [4, 5]. Therefore, how to minimize the thermally induced errors of machine tools is currently a hot research topic.

The commonly used methods to minimize thermal errors are error avoidance and error compensation [6, 7]. The error avoidance method aims to reduce or eliminate thermal errors during the design and construction phases, such as controlling the temperature rise of inner and outer heat sources, heat insulation measures, and thermal symmetric design. Although this method can improve the accuracy of machine tools, production costs will dramatically increase. With the continuous improvement of modeling theory, the studies and applications for thermally induced errors become more and more widely. The error compensation method aims to create an artificial error to eliminate the original thermal error. The error compensation method has many advantages, such as a wide field of applications at a lower cost.

Total thermally induced errors of a machine tool consist of the servo axis thermal error and the spindle thermal error. Experimental results show that the friction of screw and nut, the rotating friction of bearings, and the ambient temperature variation are the main sources of servo axis thermal error. In comparison with the above sources, the motor has little influence on servo axes because the placement is always a little far from screw in the stroke range. The rotating friction of spindle bearings, motor of spindle, and ambient temperature variation

are the main sources of spindle thermal error. The superposition of servo axis thermal error and spindle thermal error induces the comprehensive thermal error of machine tools. By paying attention to good thermal design of the machine, the thermal errors of servo axis and spindle can be countered. On the contrary, if the directions of the servo axis thermal error and the spindle thermal error are the same, the comprehensive thermal error may aggravate. Therefore, a comprehensive compensation method for thermal errors of a servo axis and spindle should be studied.

The error compensation method is a "soft technology" and has been studied for many years. Thermal error models have been established using the multiple linear regression method [8–11], artificial neural network method [12–14], thermal mode method [15], support vector machine method [16], gray model [17, 18], and time series method [19, 20]. Most of these methods are DDM (data-driven model), which need enough data to represent the input-output relationships associated with the process, and the major disadvantage of DDM is poor robustness [21]. Because it is difficult to obtain a sufficient number of representative data, when the moving information in actual machining differs from that in a thermal test, the predicted result is always poor. Besides, temperature sensors are increasingly needed to get high compensation accuracy. Therefore, it can be concluded that DDM is not the most desirable modeling method. In this paper, PBM (physically based model) is used for modeling thermal errors of a servo axis and spindle. The advantage of PBM is that the model is designed based on heat transfer theory and geometrical structure, so the forecast bias will be small.

The thermal error of *Y*-axis and radial thermal drift error of spindle in *Y*-direction are studied on a vertical machining center. They are separately modeled and experimental tests for identifying thermal characteristic parameters are carried out. Finally, the validity of PBM is verified using both experimental tests and machining.

2 Thermal error model and parameter optimization

2.1 Modeling method

The thermal errors of a servo axis and spindle are mainly due to the temperature rises of screw and spindle. An inherent relationship exists between thermal error and temperature, however is hard to be obtained. Therefore, most of the commonly used methods are DDM. DDMs need enough data to represent the input-output relationships associated with the process, and then map thermal natural phenomena to mathematical equations. Thus, if obtained data is not complete, the established model will not be suitable for all circumstances. For example, if the moving information in actual machining differs from that in thermal testing, the predicted result is always poor. However, the whole data for all circumstances is hard to be obtained. Experiments at different moving states and different temperature ranges are needed, which sometimes is even impossible. Therefore, DDM is inherently flawed and is not the most desirable modeling method.

In this paper, physically based modeling methods for thermal errors are studied. The thermal behavior of a machine tool should be analyzed if PBM is applied. The thermal behavior can be expressed by explicit or implicit mathematical formula. For example, if the screw can be discretized into M segments and the temperature of each segment is predicted, the thermal error of the whole screw can be obtained using integration. The major advantage of PBM is that it does not need sufficient data to train models. For instance, if the heat transfer model of screw is known, tests under different moving speeds and ranges for identifying parameters are not essential; instead, a test of only a moving speed and range is enough. Furthermore, the predicted value in actual machining is calculated based on a heat transfer model and the acquired thermal parameters and will not lead to bigger forecast bias.

Following Fig. 1 shows the principle diagrams of DDM and PBM.

2.2 PBM for a servo axis

2.2.1 Modeling

The screw is simplified to a one-dimensional bar because only the axial thermal deformation of screw affects the machining accuracy [22]. The screw in the stroke range is discretized into M segments, and the length of each segment is L. For a certain segment L_i of the screw in the stroke range, the frictional heat increases the temperature of L_i; at the same time, L_i conducts heat to the two sides and exchanges heat with the surrounding air. The heat transfer principle diagram is shown in Fig. 2.

The temperature of the screw at initial time is considered the same as the ambient temperature, so

$$T|_{t=0} = T_f(0) \tag{1}$$

where T is the temperature of screw, °C; T_f is the ambient temperature, °C.

For a certain segment L_i of the screw in the stroke range, the thermal equilibrium equation for L_i can be expressed as follows:

$$c \times (\rho \times L \times S) \times (T_{L_i}(t) - T_{L_i}(t-\Delta t)) = Q_{f-L_i}(t) - Q_{t-L_i}(t) - Q_{c-L_i}(t) \tag{2}$$

where c is the heat capacity of screw, J/(Kg × °C); ρ is the density of screw, Kg/m^3; S is the equivalent cross-sectional area of screw, m^2; $T_{L_i}(t)$ is the temperature of L_i at time t, °C; Δt is the sampling time, s; $Q_{f-L_i}(t)$ is the frictional heat

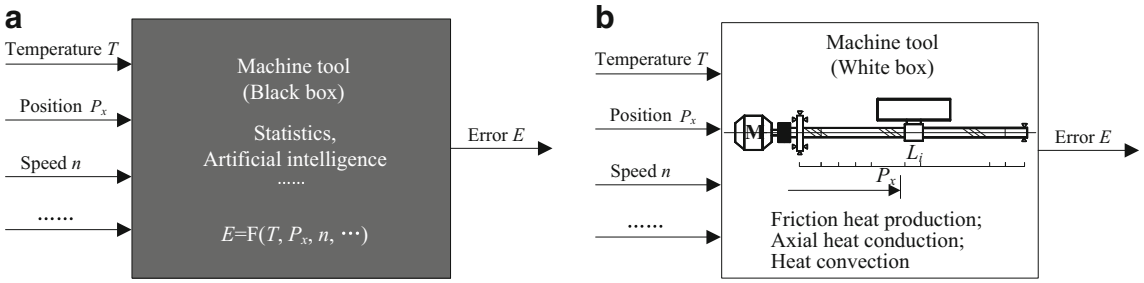

Fig. 1 **a** DDM Principle diagram. **b** PBM principle diagram

production of L_i during (t-Δt, t), J; $Q_{t-L_i}(t)$ is the axial heat conduction of L_i to both two sides during (t-Δt, t), J; and $Q_{c-L_i}(t)$ is the heat convection of L_i with the surrounding air during (t-Δt, t), J.

(1) Frictional heat production

For L_i, set Q is the heat production of L_i after one friction. The total frictional heat production $Q_{f-L_i}(t)$ during (t-Δt, t) can be expressed as follows:

$$Q_{f-L_i}(t) = Q \times N \tag{3}$$

where N is the number of frictions of L_i during (t-Δt, t).

(2) Axial heat conduction

Heat conduction is the heat transfer produced by motion or collision of a heat carrier. From a macroperspective, the heat conduction is caused by temperature gradient and the classical Fourier law in the form of differential equation describes this phenomenon [23].

$$q = \lambda \times \nabla T = \lambda \times \left(\frac{\partial T}{\partial x} j_x + \frac{\partial T}{\partial y} j_y + \frac{\partial T}{\partial z} j_z\right) \tag{4}$$

where q is the density of heat flow, J/m^2; λ is the coefficient of heat conduction of screw, W/(m × °C); ∇ is the Laplace operator; j_x, j_y, j_z are the unit vectors in x, y, z directions, respectively.

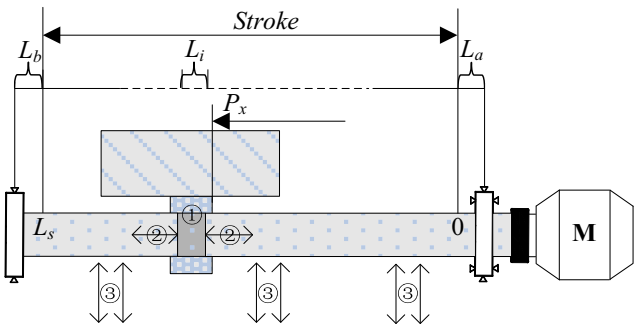

Fig. 2 Heat transfer principle diagram of screw

Since the screw is simplified to a one-dimensional bar, the heat passing through the screw cross-section in unit time is:

$$Q_{t-L_i} = S \times q = \lambda \times S \times \frac{\partial T}{\partial x} \tag{5}$$

After discretizing Eq. (5), the axial heat conduction $Q_{t-L_i}(t)$ of L_i during (t-Δt, t) can be expressed as follows:

$$Q_{t-L_i}(t) = \lambda \times S \times \frac{\left(T_{L_i}(t) - T_{L_{i+1}}(t)\right) + \left(T_{L_i}(t) - T_{L_{i-1}}(t)\right)}{L} \times \Delta t \tag{6}$$

In particular, for L_1 and L_M,

$$Q_{t-L_1}(t) = \lambda \times S \times \frac{T_{L_1}(t) - T_{L_a}(t)}{0.5 \times (L_a + L)} \times \Delta t + \lambda \times S \times \frac{T_{L_1}(t) - T_{L_2}(t)}{L} \times \Delta t \tag{7}$$

$$Q_{t-L_M}(t) = \lambda \times S \times \frac{T_{L_M}(t) - T_{L_{M-1}}(t)}{L} \times \Delta t + \lambda \times S \times \frac{T_{L_M}(t) - T_{L_b}(t)}{0.5 \times (L + L_b)} \times \Delta t \tag{8}$$

(3) Heat convection

The heat convection $Q_{c-L_i}(t)$ of L_i with the surrounding air during time (t-Δt, t) can be expressed as follows:

$$Q_{c-L_i}(t) = h \times S' \times \left(T_{L_i}(t) - T_f(t)\right) \times \Delta t \tag{9}$$

where h is the heat exchange coefficient, W/(m^2 × °C), and S' is the heat exchange area of L_i, m^2.

According to Nusselt criterion, h can be expressed as:

$$h = \lambda_a \times C \times \left(\frac{gL^3 \beta \Delta T}{\upsilon^2} \times P_r\right)^m / L \tag{10}$$

where λ_a is the heat conduction coefficient of air, W/(m × °C); C and m are the coefficients and determined by the heat source and airflow form [24]; P_r is the Prandtl number; g is the

gravitational acceleration, m/s^2; β is the expansion coefficient of air, °C^{-1}; υ is the kinematic viscosity of air, m^2/s; ΔT is the temperature difference between air and screw, °C; and L is the feature size, m.

The real-time temperature $T_{L_i}(t)$ of L_i can be obtained from Eqs. (2), (3), (6), (7), (8), and (9).

The above derivation shows that the real-time temperature field of screw can be calculated if the initial temperature $T|_{t=0}$ of screw at thermal steady state, the real-time ambient temperature $T_f(t)$, and the moving information of servo axis are known. The thermally induced error of servo axis at a certain time t can be expressed as follows:

$$E_{fd}(t) = \sum_{i=1}^{M} \alpha \times (T_{L_i}(t) - T_{L_i}(0)) \times L_i \tag{11}$$

where α is the thermal expansion coefficient of screw, μm/(m × °C).

The abovementioned PBM records the dynamic process of the thermal field of a screw. No matter how the moving state of a servo axis changes, including the moving speed, moving range, whether moving or not, the real-time thermal error of the servo axis can be obtained by Eq. (11). Compared to DDM, which does not know the thermal field of screw and needs many temperature sensors, this kind of modeling method has higher accuracy and stronger robustness.

2.2.2 Identification of parameters

In the model shown in Section 2.2.1, some parameters are difficult to determine, such as the coefficient of heat conduction α, heat exchange coefficient h, heat production Q, heat capacity c, the equivalent cross-sectional area of screw S, heat exchange area S', the length of screw outside the stroke range in the motor side L_a, and the length of screw outside the stroke range in the other side L_b. Thus, these parameters should be identified. ISIGHT is one of the best integrated CAE software and automatic parameter identification platform. This platform organizes the parameter identification process into a uniform frame [25]. The optimization program is written in MATLAB; Eq. (12) is the optimization function.

$$\min\left[F\left(c,h,\lambda,Q,L_a,L_b,S,S',\alpha\right)\right] = \sum_{u=1}^{U}\sum_{v=1}^{V}\left(E_{fd}(u,v) - E_{fdt}(u,v)\right) \tag{12}$$

where $E_{fd}(u,v)$ is the calculated thermal error of the vth test point during the uth test; $E_{fdt}(u,v)$ is the tested thermal error of the vth test point during the uth test; U is the total test times; and V is the total test points of a servo axis.

2.3 PBM for a spindle

2.3.1 Modeling

The thermally induced spindle errors consist of radial thermal drift error and axial thermal growth error. In this section, only radial thermal drift error is studied. Moreover, because of symmetrical structure in X-direction of the C-type vertical machine centers, only thermal drift error in Y-direction is modeled and the error in X-direction can be neglected. Two assumptions are given first: (1) spindle is rigid and does not bend and (2) thermal fields of both upper and lower surface of the spindle box are approximately even.

A C-type vertical machine center is simplified, and the diagrams of initial thermal equilibrium state and probable thermal deformations are shown in Fig. 3.

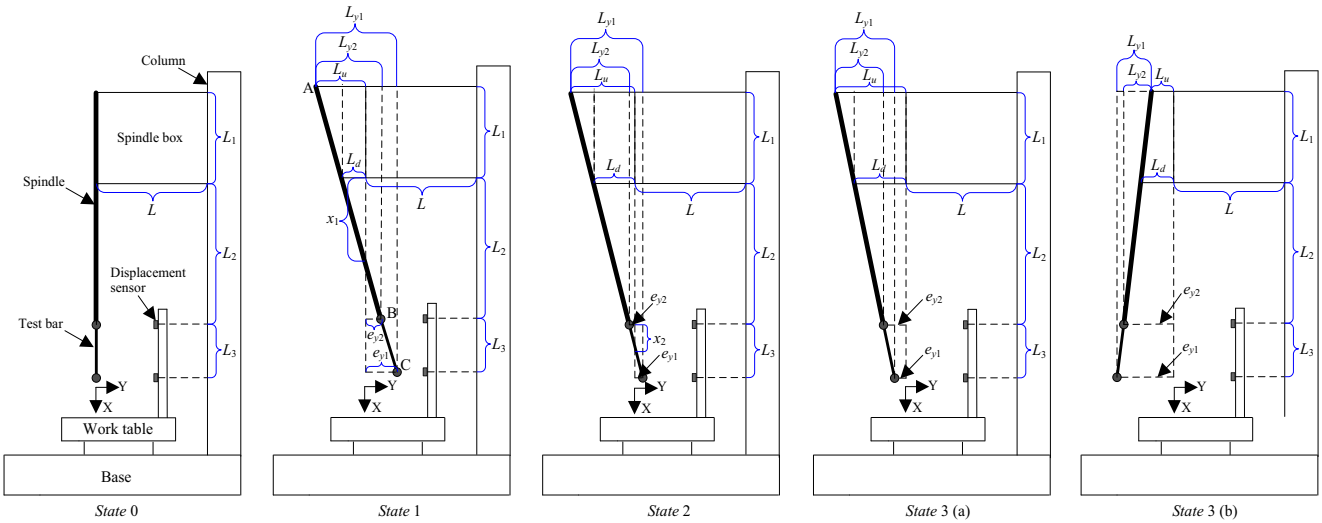

Fig. 3 Diagrams of probable thermal deformations

where L_1 is the distance between the upper and lower surface of spindle box in the vertical direction, m; L_2 is the distance between the lower surface of spindle box and the upper displacement sensor in the vertical direction m; L_3 is the distance between the upper and lower displacement sensor in the vertical direction, m; L_u is the thermal elongation of the upper surface of spindle box, m; L_d is the thermal elongation of the lower surface of spindle box, m; e_{y1} is the thermal drift error measured by the lower displacement sensor, μm; e_{y2} is the thermal drift error measured by the upper displacement sensor, μm; x_1 is the distance between the lower surface of spindle box and the crossover point, crossed by the distorted spindle and the original spindle, m; x_2 is the distance between the upper test bar and the crossover point, crossed by the distorted spindle and the original spindle, m; $L_{y1}(t)$ is the projection of AC in the horizontal plane, m; and $L_{y2}(t)$ is the projection of AB in the horizontal plane, m.

Depending on the settings of the spindle error analyzer, when the distance between the displacement sensor and the test bar becomes smaller, positive error is displayed. Three different kinds of thermal deformations exist after spindle heating:

(1) deformation 1: $e_{y1} > 0$, $e_{y2} > 0$
(2) deformation 2: $e_{y1} > 0$, $e_{y2} < 0$
(3) deformation 3: $e_{y1} < 0$, $e_{y2} < 0$

According to assumption (2), the thermal elongation errors of the upper and lower surface of the spindle box and the temperatures of the upper and lower surface of the spindle box are linearly related. The thermal elongation errors L_u (t) and L_d (t) at time t can be calculated using the temperature variations of T_u (t) and T_d (t), respectively.

$$L_u(t) = c_u(1) \times (T_u(t) - T_u(0)) + c_u(2) \tag{13}$$

$$L_d(t) = c_d(1) \times (T_d(t) - T_d(0)) + c_d(2) \tag{14}$$

where $c_u(1)$, $c_u(2)$, $c_d(1)$, and $c_d(2)$ are the coefficients to be identified.

(1) Thermal deformation 1

Equation (15) can be obtained from the triangular proportional relationship:

$$\frac{x_1}{L_1} = \frac{L_d}{L_u - L_d} \tag{15}$$

$x_1(t)$ at time t can be expressed as follows:

$$x_1(t) = \frac{L_d(t) \times L_1}{L_u(t) - L_d(t)} \tag{16}$$

From the triangular proportional relationship, e_{y1} and e_{y2} at time t can be expressed as:

$$\left|e_{y2}(t)\right| = \frac{(L_2 - x_1(t)) \times L_d(t)}{x_1(t)} \tag{17}$$

$$\left|e_{y1}(t)\right| = \frac{(L_2 + L_3 - x_1(t)) \times L_d(t)}{x_1(t)} \tag{18}$$

(2) Thermal deformation 2

Equations (19) and (20) can be obtained by triangular proportional relationship:

$$\frac{L_{y2}}{L_u - L_d} = \frac{L_1 + L_2}{L_1} \tag{19}$$

$$\frac{x_2}{L_1 + L_2} = \frac{L_u - L_{y2}}{L_{y2}} \tag{20}$$

$x_2(t)$ at time t can be obtained by substituting Eq. (7) into Eq. (8):

$$x_2(t) = \frac{L_d(t) \times (L_1 + L_2) - L_u(t) \times L_2}{L_u(t) - L_d(t)} \tag{21}$$

$e_{y1}(t)$ and $e_{y2}(t)$ at time t can be obtained by triangular proportional relationship.

$$\left|e_{y2}(t)\right| = \frac{x_2(t) \times L_d(t)}{x_2(t) + L_2} \tag{22}$$

$$\left|e_{y1}(t)\right| = \frac{e_{y2}(t) \times (L_3 - x_2(t))}{x_2(t)} \tag{23}$$

(3) Thermal deformation 3

Thermal deformation 3 contains two conditions: $|e_{y1}| < |e_{y2}|$ and $|e_{y1}| > |e_{y2}|$. For deformation 3 (a), triangular proportional relationship gives Eqs. (24) and (25):

$$\frac{L_{y2}}{L_u - L_d} = \frac{L_1 + L_2}{L_1} \tag{24}$$

$$\frac{L_{y1}}{L_u - L_d} = \frac{L_1 + L_2 + L_3}{L_1} \tag{25}$$

For deformation 3 (a), $e_{y1}(t)$ and $e_{y2}(t)$ at time t can be obtained by Eqs. (26) and (27).

$$\begin{aligned}\left|e_{y2}(t)\right| &= L_u(t) - L_{y2}(t) \\ &= L_u(t) - \frac{(L_u(t) - L_d(t)) \times (L_1 + L_2)}{L_1}\end{aligned} \tag{26}$$

$$\begin{aligned}\left|e_{y1}(t)\right| &= L_u(t) - L_{y1}(t) \\ &= L_u(t) - \frac{(L_u(t) - L_d(t)) \times (L_1 + L_2 + L_3)}{L_1}\end{aligned} \tag{27}$$

Equations (28) and (29) can be obtained for deformation 3 (b) by triangular proportional relationship:

$$\frac{L_{y2}}{L_d - L_u} = \frac{L_1 + L_2}{L_1} \tag{28}$$

$$\frac{L_{y1}}{L_d - L_u} = \frac{L_1 + L_2 + L_3}{L_1} \tag{29}$$

For deformation 3 (b), $e_{y1}(t)$ and $e_{y2}(t)$ at time t can be obtained by Eqs. (30) and (31).

$$|e_{y2}(t)| = L_u(t) + L_{y2}(t) = L_u(t) + \frac{(L_d(t) - L_u(t)) \times (L_1 + L_2)}{L_1} \tag{30}$$

$$|e_{y1}(t)| = L_u(t) + L_{y1}(t) = L_u(t) + \frac{(L_d(t) - L_u(t)) \times (L_1 + L_2 + L_3)}{L_1} \tag{31}$$

Note that the model (26), (27) obtained from deformation 3 (a) and the model (30), (31) obtained from deformation 3 (b) are identical.

PBM of spindle above derived describes the radial thermal drift errors at all probable thermal deformations. Therefore, strong robustness can be achieved whether the rotating speed of spindle randomly changed or the cooling system disturbed the spindle.

2.3.2 Criterion for determining thermal deformations

Section 2.3.1 highlights that e_{y1} and e_{y2} are functions of L_1, L_2, L_3, $L_u(t)$, and $L_d(t)$. Spindle deformation may change among thermal deformations 1, 2, and 3 in actual machining process; thus, it should be determined in real time during thermal compensation. By analyzing Fig. 3, $L_{y1}(t)$ and $L_{y2}(t)$ were chosen as the criterion for the determination of thermal deformation, and the general equations to calculate $L_{y1}(t)$ and $L_{y2}(t)$ are as follows:

$$L_{y1}(t) = (L_u(t) - L_d(t)) \times \frac{(L_1 + L_2 + L_3)}{L_1} \tag{32}$$

$$L_{y2}(t) = (L_u(t) - L_d(t)) \times \frac{(L_1 + L_2)}{L_1} \tag{33}$$

The relationship between $L_{y1}(t)$, $L_{y2}(t)$, and $L_u(t)$ was chosen for determining thermal deformations.

From deformations 1, 2, and 3 (a) $L_u > L_d$, so $L_{y1}(t)$ and $L_{y2}(t)$ assume both positive values; moreover, in deformation 3 (b) $L_u < L_d$, so $L_{y1}(t)$ and $L_{y2}(t)$ assume both negative values. Therefore, the criterion is as follows:

(1) If $L_{y1}(t) > L_u(t)$ & $L_{y2}(t) > L_u(t)$ then deformation = 1
(2) If $L_{y1}(t) > L_u(t)$ & $L_{y2}(t) \le L_u(t)$ then deformation = 2
(3) If $L_{y1}(t) \le L_u(t)$ & $L_{y2}(t) < L_u(t)$ then deformation = 3

2.3.3 Identification of parameters

The parameters $c_u(1)$, $c_u(2)$, $c_d(1)$, and $c_d(2)$ in the models presented in Section 2.3.1 need to be identified. Thermal elongation errors L_u and L_d at all three deformations can be obtained from the tested values of e_{y1_t} and e_{y2_t}. Moreover, the calculated values of L_u and L_d can be obtained from Eqs. (13) and (14). The parameter identification is carried out according to Eqs. (34) and (35) [9, 26].

$$\begin{aligned} &\min[F(c_u(1), c_u(2))] = \sum_{t=1}^{N} (L_{u\_t}(t) - L_{u\_c}(t)) \\ &lb\ (1) \le c_u(1) \le ub\ (1) \\ &lb\ (2) \le c_u(2) \le ub\ (2) \end{aligned} \tag{34}$$

$$\begin{aligned} &\min[F(c_d(1), c_d(2))] = \sum_{t=1}^{N} (L_{d\_t}(t) - L_{d\_c}(t)) \\ &lb\ (3) \le c_d(1) \le ub\ (3) \\ &lb\ (4) \le c_d(2) \le ub\ (4) \end{aligned} \tag{35}$$

where L_{u_t} and L_{d_t} are the thermal elongation errors obtained from the tested values of e_{y1_t} and e_{y2_t}; L_{u_c} and L_{d_c} are the

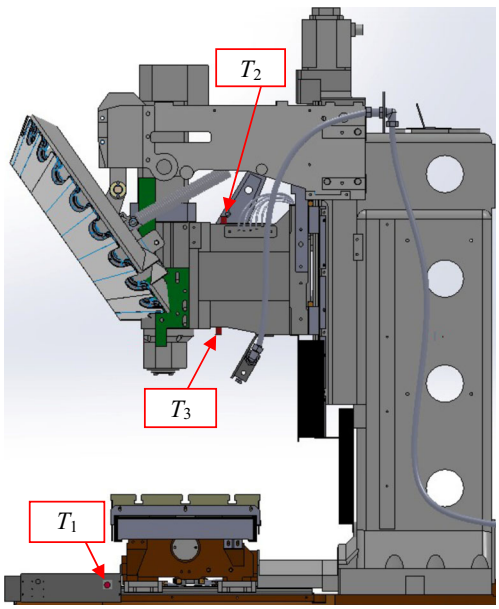

Fig. 4 The tested machine and temperature sensor positions

Fig. 5 Test of thermal errors using a laser interferometer

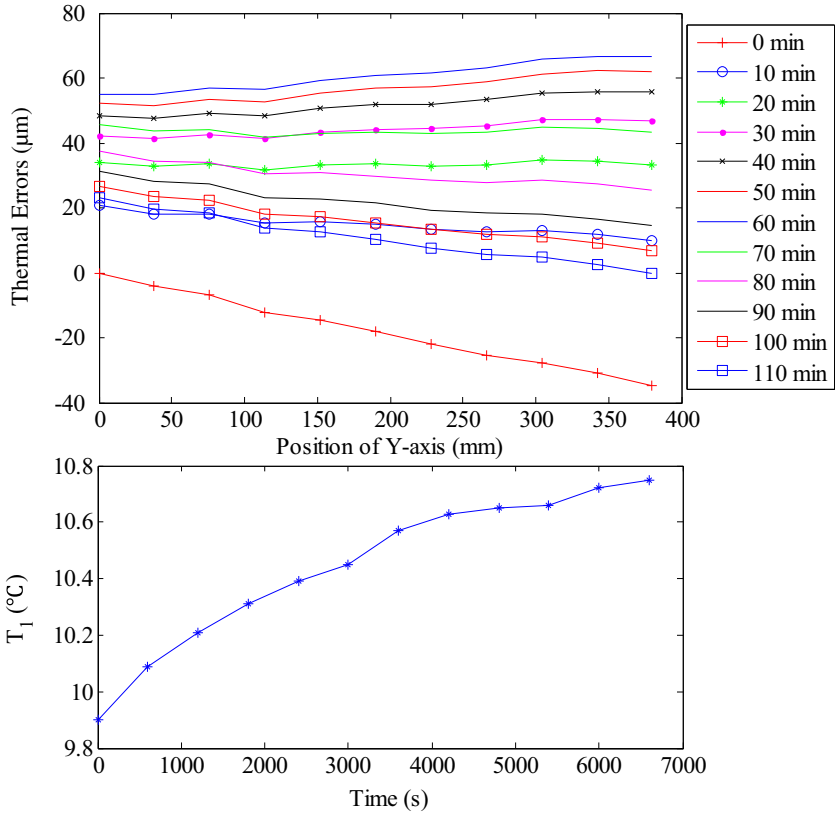

Fig. 6 *Y*-axis test results

calculated values of L_u and L_d obtained from Eqs. (13) and (14); and $lb(i)$ and $ub(i)$ are the lower and upper limitations of parameters, respectively.

3 Tests to identify the parameters

Thermal tests were carried out on a vertical machining center TC500 featured with FANUC 0*i* MD control. Maximum speed of *Y*-axis was 48 m/min; the half-closed-loop control activated the *Y*-axis and the screw was fixed on the motor side and supported on the other side. The mechanical spindle was driven by belt and its maximum rotating speed was 24,000 rpm.

Three temperature sensors, whose accuracy was ±0.1 °C (5–45 °C), were installed on the machine. Following Fig. 4 shows the positions of temperature sensors on tested machine. The temperature sensor T_1 was mounted on the bed nearby the

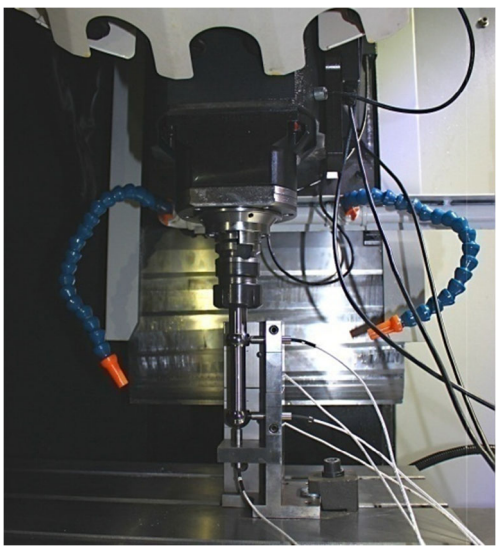

Fig. 7 Test on spindle: experimental setup

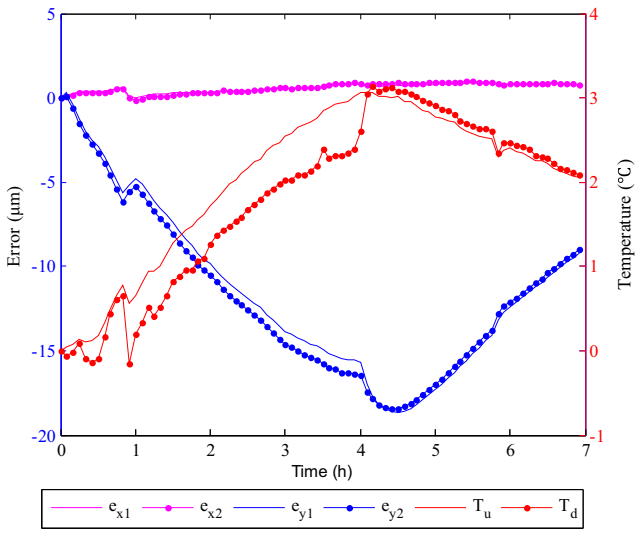

Fig. 8 Spindle test plot results

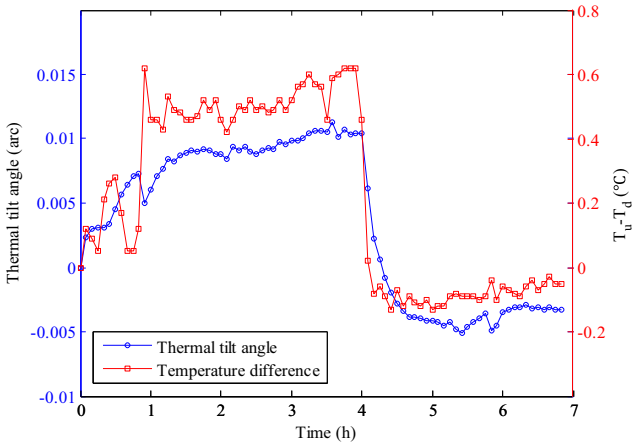

Fig. 9 Comparison between the temperature difference and the thermal angle of spindle

Y-axis; T_2 and T_3 were placed on the upper and lower surface of the spindle box, respectively. The initial temperature measured by T_1 approximately represented the initial temperature of screw, and the real-time values approximately represented the temperature T_f of the surrounding air. Measurements from sensors T_2 and T_3 were the temperatures T_u and T_d, respectively.

3.1 Tests on servo axis

Thermal errors of servo axis were measured with a laser interferometer XL80 (Renishaw Company, UK). Note that the parameter "expansion compensation of material" should be set as 20 °C to achieve the actual accuracy in any temperature. Figure 5 shows the thermal error experimental setup.

The procedure of thermal test of *Y*-axis is as follows:

(1) Firstly, test the positioning error of *Y*-axis in initial thermal steady state in the range from −10 to −390 mm, and record the value of T_1. Clearance at the test starting point is essential only in the first test.
(2) Let *Y*-axis move in the range from −10 to −390 mm at the speed of 10,000 mm/min for 10 min.
(3) Stop the movement. Test the positioning error of *Y*-axis, and record the value of T_1.
(4) Repeat steps (2) and (3) for six times.
(5) Let *Y*-axis stop at −10 mm position to cool down. Test the positioning error every 10 min until five times, and record the value of T_1.

The results of *Y*-axis test are shown in Fig. 6.

Figure 6 shows that the thermal drift error of the origin is big and reaches to 55 μm because the screw is far from the bearing on the motor side and the test starting point. In that situation, the screw discretization described in Section 2.2.1 should be carried out for the whole screw instead of considering the screw in the stroke range.

3.2 Tests on spindle

Spindle radial thermal drift errors were tested at 10000 rpm using a spindle error analyzer CPL290 (Lion Precision Corporation, USA), as shown in Fig. 7. At the same time, T_2 and T_3, and T_u and T_d were acquired. To collect data both in temperature rising and falling phases, the spindle rotated for 4 h at 1000 rpm and then was stopped for 3 h. The sampling periods for error and temperature data were both set to 10 s; Fig. 8 plots the results. Thermal drift error in *X*-direction is small due to the symmetrical structure of the machine in *X*-direction. Besides, temperature and error fluctuate at 1 and 6 h respectively due to the influx of cold outside air.

Section 2.3 showed that the thermal drift error in *Y*-direction is mainly caused by the temperature difference of the upper and lower surface of spindle box. To verify this assumption, Fig. 9 shows the comparison of temperature difference and thermal angle of spindle, where the angle was calculated by atan($(L_u$-$L_d)/L_1$). The curves of temperature difference and thermal tilt angle of the spindle are similar. Furthermore, correlation analysis was carried out and the calculated correlation coefficient between temperature difference and spindle thermal angle is 0.94, a value that validates the assumption and the proposed model.

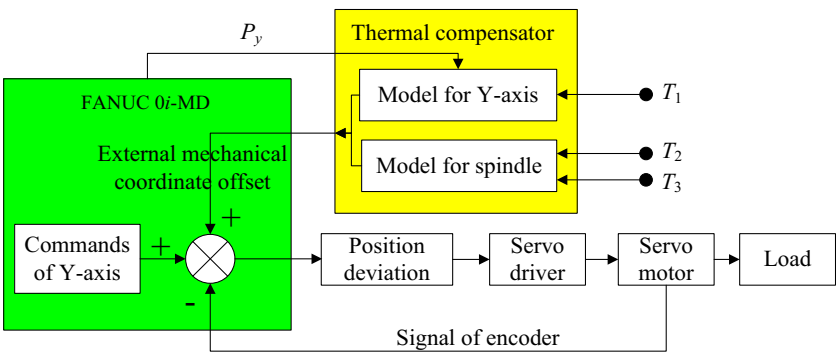

Fig. 10 Diagram of real-time compensation

4 Verifications

4.1 Communication software

Real-time compensation requires the reading of servo axis positions from CNC and the writing of compensation values to CNC. Fanuc open CNC API specifications was used to obtain these reading and writing functions. This kind of method does not need to modify the CNC hardware and software and neither the workpiece coordinate nor the machining process will be influenced. Figure 10 shows the diagram of real-time compensation.

The comprehensive thermal test and compensation software were developed in MATLAB R2014a, and the functions such as temperature acquisition, CNC communication, data analysis, modeling, and real-time compensation were also made with this software. The interface of real-time compensation is shown in Fig. 11.

4.2 Experiments

In this section, the compensation for comprehensive thermally induced errors of spindle and *Y*-axis was verified using a laser interferometer XL80: the reflector was installed on the far end of the worktable; the spectroscope was mounted on the spindle. In this way, the laser interferometer both recorded the thermally induced errors of spindle and of *Y*-axis. In other words, the tested error is the relative error of worktable and spindle in *Y*-direction. Figure 12 shows the testing equipment.

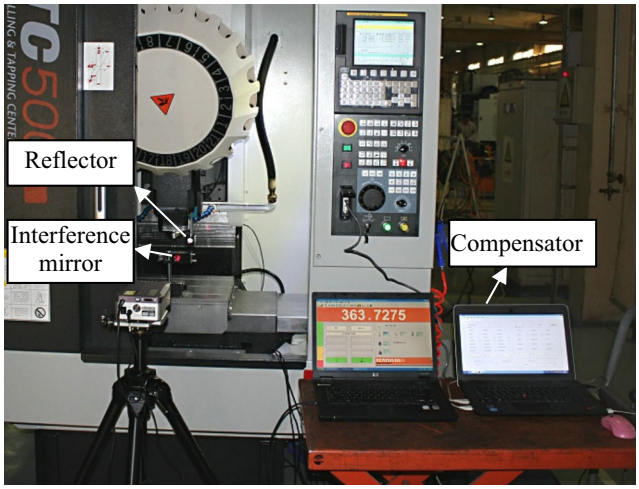

Fig. 12 Testing equipment

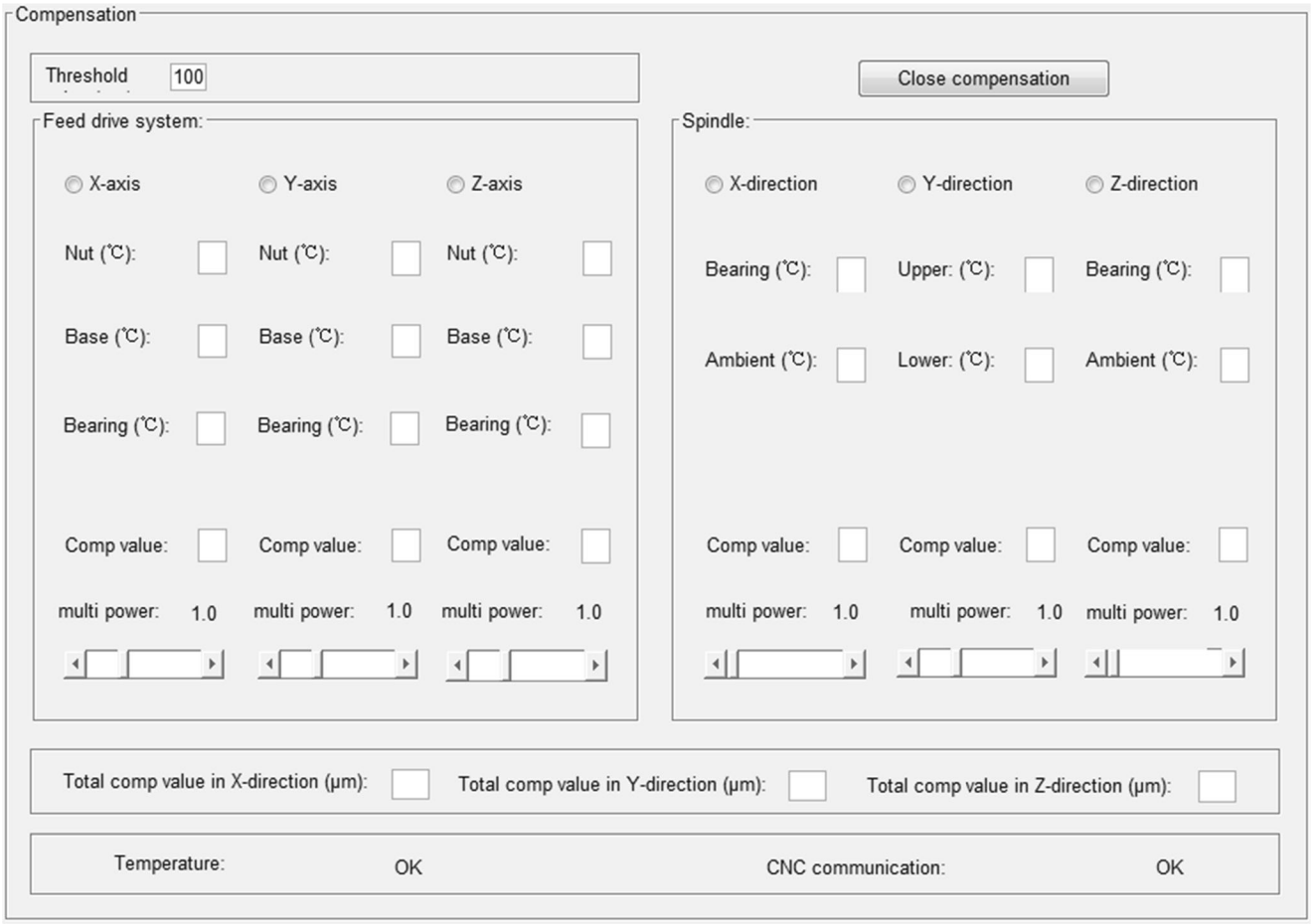

Fig. 11 Interface of real-time compensation

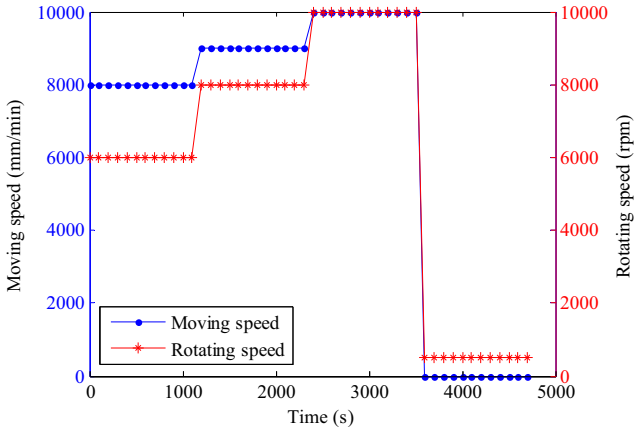

Fig. 13 Moving information in compensation tests

The procedure of compensation test is described as follows: (1) test the positioning error of *Y*-axis in an initial thermal steady state without and with compensation in the range from −10 to −390 mm first. (2) Let *Y*-axis and spindle move according to the path shown in Fig. 13, where *Y*-axis moves within the range −10 to −390 mm. (3) Measure *Y*-axis positioning error every 10 min without and with compensation. Note that clearance at the test starting point to get the thermal drift error of spindle is required only for the first test.

Figure 14 shows the experimental results. The errors without compensation contain spindle thermal drift error in *Y*-direction e_y (T_2, T_3) and thermal expansion error of *Y*-axis E_{fd} (T_1, P_y). The errors without compensation range from 34.6 to 49.6 μm, whereas the errors with compensation range from −0.4 to 5.1 μm. Note that the accuracy is high even if the moving information of Fig. 13 is changeable. Therefore, the strong robustness of PBM is verified.

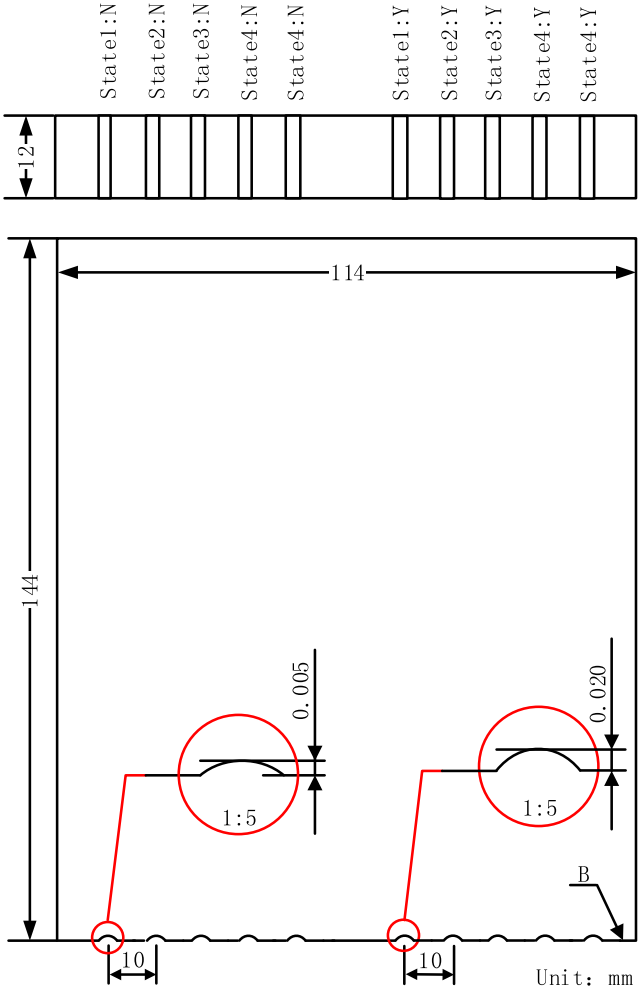

Fig. 15 Workpiece for verification

4.3 Machining

In this section, machining without and with compensation was performed for further verification of PBM. The side face of a

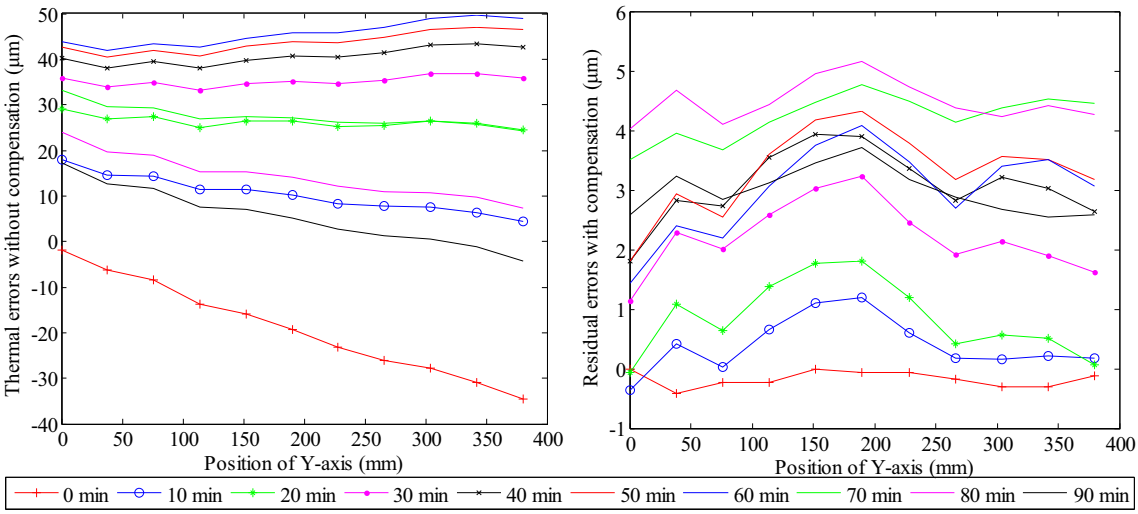

Fig. 14 Comparison without (*left*) and with compensation (*right*)

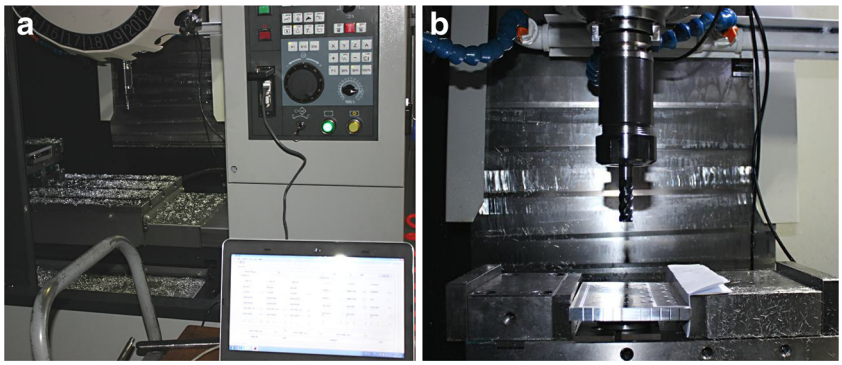

Fig. 16 **a** Machining site. **b** Machining process

rectangular workpiece was machined on the vertical machining center TC500 to evaluate by eye the differences without and with compensation. Figure 15 shows the main features of the machined workpiece.

The experiment was performed according to following steps:

(1) Open the compensator. The compensator was connected to CNC through Ethernet cable, as Fig. 16a shows.
(2) Fix the workpiece on the worktable with a jaw vice.
(3) Mill side face B using a φ12 4-edge milling cutter to guarantee its straightness and fineness.
(4) Mill one hole 5 μm width on the left side of the surface without compensation (marked as "State 1: N" as shown in Fig. 15).
(5) Open the compensator and mill one hole 5 μm width on the right side of the piece, with compensation (marked as "State 1: Y" as shown in Fig. 15).
(6) Raise the spindle. Let *Y*-axis and spindle move according to Table 1.
(7) Stop moving. Mill a 5-μm-width second hole on the left side of the piece, without compensation (marked as "State 2: N" as shown in Fig. 15).
(8) Open the compensator, and mill a 5-μm-width second hole on the right side of the piece, with compensation (marked as "State 2: Y" as shown in Fig. 15).
(9) Repeat steps (6)–(8) until five groups of holes are machined.

Figure 17 shows the machined workpiece. Note that due to the size of the *Y*-axis positioning error, the compensator also compensated it. Therefore, the actual depth of the holes on the right side was more than 5 μm.

Figure 17 shows that the micron-level thermally induced errors of servo axis and spindle can be easily observed by unaided eye. In addition, the observation of the machined workpiece without and with compensation leads to the conclusion that even if the machine moved according to the randomly changed information shown in Table 1, the accuracy stability with compensation is much better than that obtained without compensation, thus further verifying the strong robustness of PBM.

Table 1 Machining moving parameters

Number	*Y*-axis speed (mm/min)	*Y*-axis range (mm)	Spindle rotating speed (rpm)	Time (min)
1	8000	−300 to −10	2000	8
2	9000	−390 to −100	4000	10
3	10,000	−350 to −50	6000	15
4	12,000	−390 to −10	8000	15

5 Conclusions

The advantages of PBM to DDM were discussed, and PBMs for comprehensive thermally induced errors of servo axis and spindle were proposed. The compensation effects were verified using both experimental tests and machining. The salient points of this work are outlined as follows: (a) PBMs of servo axis and spindle were established, which promote the progress of modeling method for thermal errors comparing to the commonly used DDMs. (2) The comprehensive thermally induced errors of servo axis and spindle were compensated together. (3) Strong robustness of the proposed PBMs was verified, and the compensation results were still good even if the moving state of servo axis and the rotating speed of spindle randomly changed. (4) Comprehensive compensation of servo axis and spindle only needed three temperature sensors; thus, the cost is lower. (5) The test efficiency for identification of parameters is

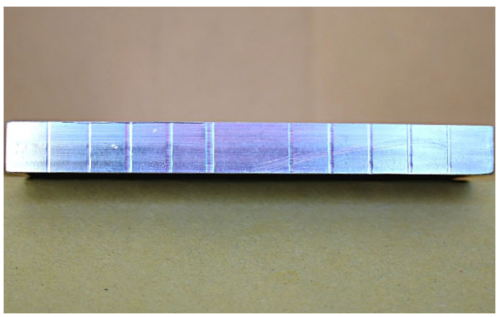

Fig. 17 The machined workpiece

higher, and only one test is needed for servo axis and spindle. Therefore, it can be concluded that presented work can be widely applied to machine tools in non-controlled temperature workshops.

It should be noted that the cutting tool is not coaxial with the spindle when the cutting tool is changed or clamped again, which would lead to the radial error of the spindle. However, this error is random and unpredictable. Therefore, if the cutting tool changes, the tool should be preseted before real-time thermal error compensation.

Acknowledgements The authors gratefully acknowledge the support of "the Fundamental Research Funds for the Central Universities (DUT16RC(3)122)" and "High-Grade CNC Machine Tool and Basic Manufacturing Equipments" Science and Technology Major Project (2014ZX04014021). Moreover, the authors thank the anonymous referees and editor for their valuable comments and suggestions.

References

1. Mayr J, Jedrzejewwski J, Uhlmann E (2012) Thermal issues in machine tools. CIRP Ann Manuf Technol 61:771–791
2. Lee DS, Choi JY, Choi DH (2003) ICA based thermal source extraction and thermal distortion compensation method for a machine tool. Int J Mach Tools Manuf 43(6):589–597
3. Zhu WB (2004) Research and application of the real-time thermal error compensation system for CNC machine tools. Dissertation, Shanghai Jiao Tong University
4. Ramesh R, Mannan MA, Poo AN (2000) Error compensation in machine tools—a review part II: thermal errors. Int J Mach Tools Manuf 40:1257–1284
5. Liu K, Liu Y, Sun MJ, Li XL, Wu YL (2016) Spindle axial thermal growth modeling and compensation on CNC turning machines. Int J Adv Manuf Technol 87(5):2285–2292
6. Ni J (1997) CNC machine accuracy enhancement through real-time error compensation. J Manuf Sci Eng Trans ASME 119:717–725
7. Yang J (1998) Error synthetic compensation technique and application for NC machine tools. Dissertation, Shanghai Jiao Tong University
8. Pajor M, Zapłata J (2011) Compensation of thermal deformations of the feed screw in a CNC machine tool. Adv Manuf Sci Technol 35:9–17
9. Lei CL, Rui ZY (2012) Thermal error modeling and forecasting based on multivariate autoregressive model for motorized spindle. Mech Sci Technol Aerosp Eng 31:1526–1529
10. Wu CW, Tang CH, Chang CF, Shiao YS (2011) Thermal error compensation method for machine center. Int J Adv Manuf Technol 59:681–689
11. Zhu J, Ni J, Shih AJ (2008) Robust machine tool thermal error modeling through thermal mode concept. J Manuf Sci Eng 130: 0610061–0610069
12. Ozkan MT (2013) Experimental and artificial neural network study of heat formation values of drilling and boring operations on Al 7075 T6 workpiece. Indian J Eng Mater Sci 20:259–268
13. Yang H, Ni J (2005) Dynamic neural network modeling for nonlinear, nonstationary machine tool thermally induced error. Int J Mach Tools Manuf 45:455–465
14. Jin ZF, Wang P (2012) Neural network–based thermal error modeling in ball screw. Modular Mach Tool Autom Manuf Tech 1:67–70
15. Yang JG, Yuan JX, Ni J (1999) Thermal error mode analysis and robust modeling for error compensation on a CNC turning center. Int J Mach Tools Manuf 39:1367–1381
16. Lin WQ, Fu JZ, Chen ZC, Xu YZ (2009) Modeling of NC machine tool thermal error based on adaptive best-fitting WLS-SVM. J Mech Eng 45(3):178–182
17. Zhang Y, Yang JG (2011) Modeling for machine tool thermal error based on Grey model preprocessing neural network. J Mech Eng 47(7):134–139
18. Li YQ, Yang JG (2006) Application of Grey system model to thermal error modeling on machine tools. China Mech Eng 17(23): 2439–2442
19. Shu QL, Li YL, Lv YS (2012) Application of time series analysis to thermal error modeling OU NC micro-grinder. Modular Mach Tool Autom Manuf Tech 12:30–32
20. Li YX, Tong HC, Cao HT, Zhang HT, Yang JG (2006) Application of time series analysis to thermal error modeling on NC machine tool. J Sichuan Univ 38(2):74–78
21. Shrestha RR, Nestmann F (2014) Physically based and data-driven models and propagation of input uncertainties in river flood prediction. J Hydrol Eng 14(12):1309–1319
22. Chen C, Qiu ZR, Li XF, Dong CJ, Zhang CY (2011) Temperature field model of ball screws used in servo systems. Opt Precis Eng 19: 1151–1158
23. Chen C (2010) Structure analysis and research on drive system thermal error model of θFXZ type CMMs. Dissertation, Tianjin University
24. Li X (2001) Real-time prediction of workpiece errors for a CNC turning center, part 2. Modeling and estimation of thermally induced errors. Int J Adv Manuf Technol 17(9):654–658
25. Du G, Chen J, Cao RJA (2010) Optimization design platform for wing turbine airfoil based on Isight. Acta Energiae Solaris Sinica 31(7):891–895
26. Xiang ST, Yang JG, Zhang Y (2014) Modeling method for spindle thermal error based on mechanism analysis and thermal basic characteristics tests. J Mech Eng 50:144–152